Polarized Cortical Tension drives Zebrafish Epiboly Movements

Amayra Hernández-Vega[1*], María Marsal[1*], Philippe-Alexandre Pouille[1*], Sebastien Tosi[2], Julien Colombelli[2], Tomás Luque[3], Daniel Navajas[3], Ignacio Pagonabarraga[4] and Enrique Martín-Blanco[1#]

1. Instituto de Biología Molecular de Barcelona, Consejo Superior de Investigaciones Científicas

Parc Científic de Barcelona, Baldiri Reixac 10-12, 08028 Barcelona, Spain

2. Advanced Digital Microscopy Core Facility, Institute for Research in Biomedicine - IRB Barcelona

Parc Científic de Barcelona, Baldiri Reixac 10-12, 08028 Barcelona, Spain

3. Institute for Bioengineering of Catalonia, Universitat de Barcelona, and CIBER Enfermedades Respiratorias

Parc Científic de Barcelona, Baldiri Reixac 10-12, 08028 Barcelona, Spain

4. Departament de Física Fonamental, Facultat de Física, Universitat de Barcelona

Martí i Franquès 1, 08028 Barcelona, Spain

* These authors contributed equally to this work

\# Corresponding author: Enrique Martin-Blanco, embbmc@ibmb.csic.es

ABSTRACT

The principles underlying the biomechanics of morphogenesis are largely unknown. Epiboly is an essential embryonic event in which three tissues coordinate to direct the expansion of the blastoderm. How and where forces are generated during epiboly and how these are globally coupled remains elusive. Here we developed a method, Hydrodynamic Regression (HR), to infer 3D pressure fields, mechanical power and cortical surface tension profiles. HR is based on velocity measurements retrieved from 2D+T microscopy and their hydrodynamic modeling. We applied HR to identify biomechanically active structures and changes in cortex local tension during epiboly in zebrafish. Based on our results, we propose a novel physical description for epiboly, where tissue movements are directed by a polarized gradient of cortical tension. We found that this gradient relies on local contractile forces at the cortex, differences in elastic properties between cortex components and force passive transmission within the yolk cell. All in all, our work identifies a novel way to physically regulate concerted cellular movements that will be fundamental for the mechanical control of many morphogenetic processes.

INTRODUCTION

The construction of complex functional structures during morphogenesis results from the unfolding of the developmental program of individual cells. Importantly, morphogenesis does not only rely on a tight regulation of gene expression and cell communication but also depends on fundamental physical principles (Aigouy, Farhadifar et al., 2010, Desprat, Supatto et al., 2008, Grill, 2011, Kiehart, Galbraith et al., 2000, Lecuit, Lenne et al., 2011, Lepage & Bruce, 2010, Martin, 2010, Pouille, Ahmadi et al., 2009, Rauzi & Lecuit, 2009). The stereotyped tissue movements involved and the embryo optical accessibility makes zebrafish epiboly ideal for exploring mechanical coordination during morphogenesis (Behrndt, Salbreux et al., 2012, Concha & Adams, 1998, Keller, Davidson et al., 2003).

Epiboly is a conserved early embryonic morphogenetic movement that involves a striking physical reorganization characterized by the thinning and spreading of cell layers. Epiboly initiates when the Enveloping Layer (EVL), an external epithelial sheet, the Deep Cells – DCs, a spherical cap of blastomers centered on the animal pole of the embryo over the yolk cell and the External Yolk Syncytial Layer (E-YSL), a specialized region at the yolk surface positioned ahead at the EVL, undergo cortical vegetalward movements. These are associated to the shortening of the rest of the yolk surface (Yolk Cytoplasmic Layer - YCL) and the doming up of the internal yolk. Epiboly ends by the closure of the blastoderm at the vegetal pole covering the yolk cell (Kimmel, Ballard et al., 1995, Rohde & Heisenberg, 2007, Solnica-Krezel, 2006) (**Figure 1a**).

Biomechanical studies, however, experience a major limitation, that is the difficulty to directly measure forces *in vivo* and several methods have been developed to measure the mechanical properties of living cells. So far, however, they cannot be readily applied to whole developing organisms. Exceptions are the use of laser microsurgery (Toyama, Peralta et al., 2008) and the use of genetically engineered mechanical biosensors (Grashoff, Hoffman et al., 2010). Alas, such techniques are intrusive, fall short of quantitative characterization (e.g. laser cuts cannot distinguish active and passive responses (Rodriguez-Diaz, Toyama et al., 2008)) and cannot provide a global biomechanical representation of morphogenesis.

We have developed a novel non-intrusive method that we refer as Hydrodynamic Regression (HR), which can accurately and globally estimate the spatio-temporal profile

of mechanical power and cortical tension in living organisms. It relies in considering that in deforming tissues during morphogenesis forces are balanced and stresses are continuous at the cortex / fluid interface. This physical principle (boundary condition) has been shown to apply at the single-cell embryo level (Niwayama, Shinohara et al., 2011) and on multicellular epithelia in gastrulating embryos (He, Doubrovinski et al., 2014). HR is mesoscopic and, although it does not infer the mechanical properties of single cells, it identifies the regions where mechanical stress and power concentrate during tissue rearrangements. Importantly, it does not demand restrictive assumptions either on the mechanical nature of the cortex under stretch or on the physical properties of the embedding fluids. Thus, it can be applied to any morphogenetic process providing two conditions are met: 1) The geometry / shape of the tissues involved can be extracted from images and modeled and 2) The flows around the cortex occur at low Reynolds number, where inertia is negligible, which is the case for most biological processes (He et al., 2014, Niwayama et al., 2011).

We applied HR to study epiboly global biomechanics and estimated the topography and temporal evolution of mechanical power and surface stresses of the embryo. These inferred parameters were validated and confirmed by laser microsurgery, microrheology and Atomic Force Microscopy (AFM). In first place, we concluded that HR is suitable to explore the biomechanics of morphogenetic processes driven by the reorganization of cells or sheets of cells of finite width surrounded by fluids. In countless models, this may most probably be the case. Secondly, the HR analyses and *in silico* modeling let us suggest that epiboly mechanics and kinematics could be simply explained as a result of the integration of the contractile activity of the E-YSL and the differential elastic properties of the EVL and the yolk surface. A tension imbalance will build up across the opposite sides of the E-YSL during epiboly, enabling it to proceed (at least from 50 % onwards). These novel predictions were tested *in silico* and experimentally confirmed by interfering in Misshapen expression (a regulator of myosin contractility active during epiboly progression (Koppen, Fernandez et al., 2006)) and reducing E-YSL contractility. Our new biomechanical model, in contrast to previously suggested models (Behrndt et al., 2012), accounts for all known features of epiboly kinematics.

RESULTS

Global kinematics of Zebrafish Epiboly

To perform an analysis of epiboly biomechanics is essential first to define the kinematic properties of the cortical vegetalward movements of the EVL, DCs and E-YSL leading to embryo closure (see **Figure 1a**). Experimental kymographs of the embryo surface along the animal to vegetal axis (φ axis) were extracted from 2D time-lapse meridional sections, perpendicular to the dorso-ventral axis (**Figure 1b** and **Video EV1**). They showed a sustained displacement of the EVL / yolk margin position φ*, whose speed v* continuously increased and that could be fitted, after crossing the equator (v_0), to the function $v_\phi = v_0 / \sin \phi^*$ (**Figure 1c** and see **Appendix Note S1)**. Kymographs also showed that the local surface speed decreased exponentially from the EVL / yolk margin towards the vegetal pole (**Figure 1d**). This decay outlined two domains, a proximal one ahead of the EVL (~E-YSL) undergoing progressive constriction (see **Appendix Figure S1**) and a mostly static distal area.

The proximal E-YSL constitutes a morphologically distinguishable region with a highly convoluted membrane (Betchaku & Trinkaus, 1978, Cheng, Miller et al., 2004) (**Figure 1e**). In the E-YSL, actin was conscripted within and beneath wrinkles (**Figure 1f**) underlined by nestled mitochondria (see also (Popgeorgiev, Bonneau et al., 2011)) (**Appendix Figure S2**). Importantly, the width of the E-YSL ($\delta\phi$) and the velocity of the EVL / yolk margin v* were inversely paired ($v^* \sim 1 / \delta\phi$) at all times. This pairing was just qualitative up to reaching the equator (v_0), while quantitatively match theoretical kymographs after 50 % (**Figure 1c**).

In parallel to these cortical (EVL, DCs and E-YSL) movements, we observed that the internal yolk granules undergo stereotyped motions. They spin symmetrically around a transverse annular axis creating a torus of vortices (**Figure 2a** and **Video EV2**). As epiboly progressed, the centroids of these vortices move gradually towards the cortex and the vegetal pole (**Figure 2b-d**). Importantly, they parallel the displacement of the edge of the EVL along the ϕ axis towards the vegetal pole, which after 50 % epiboly showed a constant velocity of 200 μm/hour (z axis) (**Figure 2e**).

In summary, during epiboly the EVL leading edge movements, the shrinking and displacement of the E-YSL and the stereotyped vortices of the yolk granules are remarkably coordinated and seem mechanically coupled.

Development of a non-invasive method, Hydrodynamic Regression, to determine mechanical stress and power patterns

Although some information on the power sources for epiboly is available (Cheng et al., 2004, Koppen et al., 2006), how the different elements involved in tissue spreading are mechanically coordinated remains unexplored. To study this coupling we developed a mesoscopic method able to dynamically infer cortex stress patterns and mechanical power maps of general applicability (Hydrodynamic Regression - HR).

Method Rationale

The cortex in a biological system can be mesoscopically described as a continuous quasi-2D structure under tension embedded in viscous fluids. As such, we reasoned that the local differences in surface tension when the cortex expands or contracts could be estimated from the shear stress at its interface with the fluids. These stress values, could themselves be indirectly inferred by analyzing the flows in the surrounding media (**Figure 3a**). Therefore, by analyzing the velocity fields of embedding fluids should be in principle possible to infer the overall spatio-temporal distribution of the 2D out-of-equilibrium cortical tension, τ (see below). Theoretical considerations and derivations are fully detailed in **Appendix Note S2**.

Method implementation

To implement HR, we have first to determine the velocity fields of the media surrounding the tissue/cortex. This can be done by employing bright field transmission or two-photon confocal microscopies live and estimating tissue kinematics by Particle Image Velocimetry (PIV) (Supatto, Debarre et al., 2005). In a second step, we model the fluid motions distributing force dipoles (Stokeslet pairs) of variable strength β_e perpendicular to the cortex according to its particular geometry (a given number, N_e, at a distance δ away from each other) (**Figure 3b**). These models assume that in developmental processes, fluids at small strain rates behave as incompressible Newtonian fluids at low Reynolds number (Cartwright, Piro et al., 2009). Biological fluid dynamics can then be described by a linear continuity equation, ensuring volume conservation, and the linear Stokes equation

$$\mathrm{div}\ \mathbf{V} = 0 \quad (1)$$

$$\nu\ \Delta\mathbf{V} = \mathbf{grad}\ P \quad (2)$$

with ν being the shear viscosity, **V** the velocity field, Δ the Laplace operator, **grad** the gradient and P the mechanical pressure. The linear combination of the fluid flows generated by the force dipoles let model the 3D velocity fields (strain rates). Third, we used regression analysis to fit the analytical models to the velocity fields. At each time point a Monte Carlo scheme was used to determine β_e minimizing the mean square error (MSE) between experimental and theoretical fields. The mechanical pressure was determined from these same values. Last, considering the fluid strain rates and the mechanical pressure, we inferred the fluid shear stress, the local values of τ, the average surface tension and the cortical mechanical power Π, *i.e.* the rate of mechanical energy per unit of time (**Figure 3c**). Performing HR over time gave access to the spatio-temporal evolution of both, cortical stresses and mechanical power maps.

The pipeline used to infer the mechanics of the cortex and its surrounding fluids by HR is shown in **Figure 3d**. The workflow and protocols involved are described in **Appendix Note S2** and a flow simulation software suite with step-by-step details is provided in **Appendix Note S3**.

In principle, HR can be applied to different scenarios, materials and geometries. To verify this versatility we applied the method to diverse structures with known or easily predictable mechanical behaviors. We examined the reaction of the yolk surface of the zebrafish embryo to laser injury employing planar cortex (PC) models with stokeslet pairs distributed on a 2D square grid. Further, we evaluates a spherical fluid droplet sedimenting in an immiscible liquid building spherical cortex (SC) models with evenly distributed stokeslet pairs around one main axis on a spherical shell with cylindrical symmetry (**Figure 3e** and **Appendix Note S4**). In both cases, HR faithfully inferred mechanical pressure fields, power and surface tension maps from experimental velocity fields (see **Appendix Figures S3** and S**4** and **Video EV3**).

Epiboly Biomechanics

To understand the biomechanical behavior of the early zebrafish embryo we studied the mechanical properties of the yolk and its cortex and employed HR to identify the power sources guiding and/or contributing to epiboly and to evaluate their dynamics.

Yolk mechanical properties

We assessed the mechanical properties of the yolk by studying its rheological behavior recording the thermal fluctuations of microinjected fluorescent nanoparticles (Daniels, Masi et al., 2006). Images of yolk-injected nanoparticles were obtained and the position of their centroids, their trajectories and the two-dimensional mean square displacement (MSD) of each particle were computed. We found that the MSD exhibited a proportional dependence on time lag consistent with Newtonian fluid behavior and a viscosity of 129 mPa·s (**Figure 4a**). This viscosity of the yolk is thus in the same order to that recently determined for *Drosophila* (286 mPa.s) (He et al., 2014). Considering this viscosity, the speed of the yolk flows (epiboly progression rates - 200 μm/hour), the yolk density (similar to water ~ 1.074 g/cm^3) (Fujimura, Inoue et al., 2007) and the size of the embryo (~ 350 μm of radius), we calculated a Reynolds number for the yolk in the order of 10^{-7} (as in *Drosophila* (He et al., 2014)), a very low value.

We then performed a direct quantification of the yolk cortex viscoelastic properties. Atomic Force Microscopy (AFM) was employed to acquire local surface tension measurements on living whole embryos (see Methods and **Appendix Note S5**). The viscoelasticity of the cortex was assessed applying low amplitude (100 nm) multifrequency oscillations composed of sinusoidal waves of different frequencies (0.35 – 11.45 Hz). Cortex rheology was dominated by an elastic-like behavior with the viscous modulus ~5 times lower than the elastic modulus (**Figure 4b**). Moreover, no significant frequency dependence was found for any of these moduli in the experimental time window. As the ratio between the viscous and elastic moduli is expected to drop with decreasing frequency, our rheological data indicated that at a time scale of minutes the cortex, with an apparent elastic modulus *G'* of ~ 100 Pa (see Equation 6, Methods), behaves as a very soft solid in the range of the softest biological materials (Butcher, Alliston et al., 2009, Discher, Mooney et al., 2009).

Last, from the measured relaxation times determined by AFM we estimated the effective cortex viscosity at long-time scales (fluid-like response) in the order of $\eta_c \sim 10$ Pa.s. This implies that the ratio between the typical traction in the cortex at long times and the stresses associated to the measured flows of the fluid is just about $\eta_c w / \eta R \sim 0.1$, where w stands for the cortex width (1 – 4 μm) (Rawson, Zhang et al., 2000), R the characteristic embryo size and η the yolk viscosity. In conclusion, the yolk content can be considered a viscous Newtonian fluid with low Reynolds number and the yolk

surface behaves at the time scale of epiboly movements as an extremely soft solid. Importantly, the magnitudes of the cortical and yolk fluid tractions were truly comparable.

Epiboly mechanical power sources

We applied HR to uncover the spatiotemporal pattern of mechanical power during epiboly. To do so, experimental 2D velocity fields from time-lapse videos of embryos meridional sections employing yolk granules movements as a reference were determined by PIV. Then, simulated 3D velocity fields were generated from a SC model with Stokeslet pairs distributed on five concentrical spherical shells adjusted to the motion symmetry and the embryo cortex. These theoretical fields were fitted by regression analysis to the experimental fields (**Figure 4c** and **Video EV4**).

We found that at the epiboly onset, the active power mainly maps to the blastoderm. Later, a distinct high power domain arises under the cortex between 50 and 60 % epiboly at the position and time of the ingression of DCs. Last, once the EVL front crosses the equator, the largest mechanical power concentrates to the actomyosin-rich E-YSL, while the EVL adjacent cells display negative power densities opposing deformation. The EVL cells and DCs near the animal pole remain a weak power source (**Figure 4d** and **Video EV5**). At all times, the yolk always displays very low mechanical energy dissipation.

Cortical Stress Patterns

HR also enabled to analyze the spatio-temporal progression of local surface tension by mapping animal to vegetal (AV) and circumferential (CC) cortical stresses as a function of time (**Figure 4e** and **Video EV6**). We found that at the initiation of epiboly both, AV and CC stresses show an even distribution at the surface of the embryo. As epiboly progresses, however, a vegetalward-oriented gradient of CC stress is built up throughout the EVL and the yolk, while the AV stress displays a complex distribution. From animal to vegetal, diminishes with time at the animal pole, dramatically rises at the EVL front, drops at the E-YSL and increases again towards the vegetal pole. As a result, at the E-YSL after 50 % epiboly, the difference between AV and CC stresses sustained minimum negative values. In contrast, the stress difference in the adjacent EVL cells was positive and maximum. Summing up, a positive gradient of tension progressively develops at the yolk surface towards the vegetal pole from 50 % up to the end of epiboly. This gradient is more pronounced for the CC component.

To verify the predicted axial tensional gradient, we employed targeted laser microsurgery (Colombelli, Besser et al., 2009) (**Appendix Figures S5** and **S6** and **Appendix Note S6**). We found that the experimental disruption in the AV or CC directions of the yolk actomyosin cortex at the E-YSL resulted in an immediate recoil, with exponentially decaying speed (see also (Behrndt et al., 2012)). This let measuring the relative magnitude and directionality of local surface tensions (**Appendix Figure S7** and **Video EV7**). Significantly, the differences between AV and CC tension at each time point precisely replicated the stress differences estimated by HR (**Figure 5a**). Thus, the inferred temporal and directional pattern of tension at the E-YSL was confirmed. Equally, the predicted vegetalward AV tension gradient at the yolk surface was also confirmed at different stages by laser microsurgery at different distances from the EVL / yolk margin (**Figure 5b**).

Stress-graded profiles were further verified by AFM. We measured force-indentation curves at the yolk surface and found that they showed a perfect match to a "liquid balloon" model. This is a viscoelastic mechanical model representing a viscous liquid surrounded by an elastic cortex under mechanical stress (Evans & Yeung, 1989, Krieg, Arboleda-Estudillo et al., 2008, Lomakina, Spillmann et al., 2004). By fitting this model to the data we calculated absolute values of cortical tension (T_c) for the yolk membrane in the order of 100 pN / µm (**Figure 5c**). Performing this analysis at two different positions, 50 - 100 µm ahead of the EVL and at the vegetal pole detected after 50 % epiboly a significant long-range positive gradient of tension. Remarkably and unequivocally also pointed to the presence of tension at the vegetal pole (**Figure 5d**). These results are consistent with the short-range gradient inferred by laser cuts in agreement with the HR analysis.

In short, the predicted yolk surface stress gradient and dynamics were accurately supported by AFM and laser microsurgery.

Mechanically relevant elements leading epiboly movements

Overall, epiboly kinematics suggest that the EVL behaves mesoscopically as a homogeneous deformable sheet, that the E-YSL shrinks specially after 50% epiboly, and that the rest of the yolk cell membrane is mostly un-stretchable and kept under increasing tension. Indeed, the observed spatial and temporal differences in surface speed can be consequence of the non-homogeneous stiffness of the cortex. We

evaluated this option analyzing the cortex displacement in response to laser cuts on the yolk membrane. After recoil, the geometrical center of cuts parallel to the EVL consistently shifted towards the vegetal pole (**Figure 6a**). These data emphasize the difference of stiffness between the EVL (softer) and the yolk (stiffer) surfaces. This difference correlates with previous analysis of micro-elasticity using Brillouin Scattering Spectroscopy, which also revealed the relative higher stiffness of the yolk versus the blastoderm at early cleavage stages (Fujimura et al., 2007).

Differences in cortex stiffness may be relevant for tissue expansion and we hypothesize that epiboly, at least after 50 %, will be just reliant on the active contraction of the E-YSL and directed towards the vegetal pole as a reaction to the difference of stiffness between the animal (EVL) and vegetal (yolk) domains, which would establish a cortical tension gradient (**Figure 6b**). To assess this hypothesis we simulated epiboly *in silico*. This simulation took into account the experimental kinematics and assumed both, an exponential decay of the cortical contractility along the φ axis (in accord to the observed exponential decay of speed of the EVL / yolk margin) and that the EVL and the yolk behave as materials of different stiffness (see **Appendix Note S7**). Simulations precisely recapitulated, at least from 50 % epiboly onwards, most of the kinematic and mechanical parameters associated, the yolk internal vortices, and the mechanical power and patterns of surface tension at the cortex (**Figures 6c** and **6d** and **EV Videos 8** and **9**). Simulations also rendered a remarkably accurated profile for the speed of the EVL front displacement along the φ axis, slow first up to reaching the equator and much faster afterwards.

The mechanical simulations predict that interfering with the contractile capabilities of the E-YSL will result in a dramatic reduction in the speed of the advancing front and, in practical terms, in epiboly completion failure. Importantly, if we abolished the E-YSL shrinkage, simulations provided an aberrant regime for the speed of the EVL front with a progressive decline from 50 % epiboly onwards (**Figure 7a**).

We experimentally tested these inferences by genetically interfering in Msn1 expression. Msn1, an ortholog of the *Drosophila* Ste20-like kinase Misshapen, is a well-characterized mediator of E-YSL contractility. Actin and phospho-myosin 2 failed to be recruited at the YSL in morphants and the EVL cells at the margin do not stretch longitudinally, while ZO-1 accumulation (septate junctions) was not affected (Koppen et al., 2006). We addressed the role of *msn1* in the E-YSL injecting morpholinos in the

yolk at the sphere stage. This resulted, as previously described, in epiboly´s slowness and arrest with 50% penetrance. We performed a kinematic and mechanical analysis of *msn1* yolk morphants and found that the failure on E-YSL contractility was associated to a strong reduction in the speed of progression of the EVL front mostly after 50 % epiboly (**Figure 7b** and **Video EV10**). We further found by HR that power at the E-YSL was critically compromised and that stress gradients along the cortex were essentially abolished (**Figures 7c** and **7d**).

In short, simulations and experimental interferences in E-YSL contractility show a remarkable correlation strongly supporting that epiboly kinematics and mechanical behavior can be minimally described by 1) the contractile capabilities and gradual change of dimensions of the E-YSL and 2) the dissimilar elastic properties of the EVL and the yolk surface (**Figure 6b**).

DISCUSSION

We have performed a detailed study to determine the up to now elusive, major force-generating elements driving zebrafish epiboly (Cheng et al., 2004, Solnica-Krezel & Driever, 1994). We revealed several significant evidences: 1) both, the yolk surface (this manuscript and (Behrndt et al., 2012)) and the EVL tissue (Campinho, Behrndt et al., 2013) display elastic behavior at short time scales. This elastic response is sustained all throughout epiboly; 2) the yolk cell membrane behaves as an extremely soft solid; 3) the yolk content is fairly viscous and incompressible and flows at very low Reynolds number with negligible inertia and 4) the magnitudes of the cortical and yolk fluid tractions are comparable and of equivalent order. Further, we generated a theoretical approximation to the embryo as a tensile cortex of spherical shape (SC) surrounding a viscous fluid. Applying Hydrodynamic Regression (HR) to this SC model, we fitted a unique velocity and mechanical pressure field to experimental 2D+T time-lapses and from here we built a minimal mechanical model of epiboly.

HR is a non-invasive method able to quantitatively infer dynamic mechanical parameters (mechanical power and surface/cortical tension) from *in vivo* imaging. As it stands, the method can be applied to any deforming tissue and, with minor modifications, be extended to full 3D analysis. Consequently, HR may become

instrumental in the quantitative study of cell and tissue mechanics during embryonic development as well as in physiological and pathological processes. An extended discussion on the HR method applicability and restrictions is presented in **Appendix Note S8**.

HR provides relative values for mechanical parameters such as stress distributions and these can be extremely relevant in morphogenetic models, which mostly rely on tissues dynamic balance. The ability of accurately inferring mechanical power patterns and surface tension profiles *in vivo* in whole organisms will enable the exploration of the genetic and cellular mechanisms that account for morphogenesis biomechanics. Cytoplasmic streaming has been observed in large plant cells like Chara (Yamamoto, Shimada et al., 2006) (Goldstein, Tuval et al., 2008), in *C. elegans* (Wolke, Jezuit et al., 2007) and in the mice oocyte (Yi, Unruh et al., 2011). Velocity fields have been studied and compared to kinematic models and flows have been linked either to specific molecular motors or to stress anisotropies at the surface. However, in these works, the distributions of power and/or stress have not been inferred. HR could thus be a very useful method to uncover mechanical parameters distribution in these models.

In its application to epiboly, HR enabled to estimate not only mechanical power and provide insight in the effective surface tension variations but also to reach a global concerted representation of epiboly in which cell movements can be explained as a response to mechanics. Before surpassing the equator, an active role for the EVL and DCs on epiboly is supported by the mechanical power at the blastoderm (see **Figure 4d**) and the stresses at the embryo surface (see **Figure 4e**). EVL and DCs early activity is instrumental for epiboly progression (Concha & Adams, 1998, Koppen et al., 2006, Trinkaus, 1963, Warga & Kimmel, 1990). From 50 % onwards, however, we showed through simulations and experimental interference that polarized tensional properties of the yolk surface and the EVL altogether with the contractile capability of the E-YSL [latitudinal (CC) and longitudinal (AV)] are sufficient to explain both surface and inner movements (see model in **Figure 6b**). The gradient of tension is validated by our own laser cuts (**Figures 5** and **6a**), together with those described (Campinho et al., 2013) for the yolk and EVL marginal cells. No differences in the recoiled velocity between parallel (AV) and perpendicular cuts (CC) are observed in the marginal EVL cells at the beginning of epiboly. However, as epiboly progressed, AV tension increased (parallel cuts) while CC tension decreased in the EVL cells. Thus, a difference between AV and

CC tension, being AV higher than CC, was generated over time. In the yolk, however, the differences between AV and. CC tension were opposite to those of the EVL cells. This model is further backed by the documented preferential orientation of EVL cells under anisotropic tension in the AV direction (Koppen et al., 2006). It is also in agreement with recent observations pointing to the EVL as a continuous elastic medium in which tensions and elastic deformations occur at appropriate length scales [see (Campinho et al., 2013)]. This last issue is consistent with equivalent observations in *Fundulus* (Weliky & Oster, 1990).

It has been suggested, alternatively, that epiboly may be described as the result of the combined activities of cable-constriction and flow-friction motors (Behrndt et al., 2012). In this opposing scenario, tissue deformation would be driven by the ability of the cortical actomyosin ring at the E-YSL to contract and generate active tension, while an additional pulling longitudinal force in the yolk will be generated by a regime of intermediate friction acting against an actomyosin retrograde flow. This cortical-friction motor proposition derives from a theoretical description of YSL actomyosin network dynamics and it has not been experimentally tested. It implies that the actomyosin ring, which is mechanically connected to the EVL on its animal side, has a free boundary on its vegetal side. This assumption is essential for the model and demands that the surface tension from the contractile ring towards the vegetal pole should decrease towards zero. We found, however, that laser microsurgery in the E-YSL unequivocally pointed to an oriented gradient of AV tension from the EVL / yolk margin towards the vegetal pole (**Figure 5c**). Further, our measurements of surface tension (T_c) by AFM *in vivo* explicitly revealed a non-null surface/cortical tension at the vegetal pole, which increased with time (**Figure 5e**). Therefore, the vegetal boundary of the E-YSL is not mechanically free, as it was claimed (Behrndt et al., 2012), but linked to the tense yolk membrane. In these circumstances, the tension originated by the constriction of the actomyosin ring (at the E-YSL) will be conveyed by the yolk cell membrane towards the vegetal pole. Hence, for epiboly progression, a flow-friction motor would be, in principle, needless.

In our view, the failure to detect tension at the vegetal pole by laser microsurgery (Behrndt et al., 2012), while we readily detect a significant surface tension with AFM strongly suggests that the yolk surface/cortical tension is indeed sustained at the pole by the elastic membrane itself and not by the underlying cortex. Remarkably, considering

the notable fitting of our simulations, any potential anisotropy in material properties of the yolk membrane seems not to be mechanically relevant. In this context, the role of the observed yolk cortical retrograde flows of actin and myosin might be, not to provide a friction force, but to replenish actin and myosin, which undergo rapid turnover at the contractile E-YSL.

In summary, by applying HR we have defined the spatio-temporal evolution of local cortical tensional stresses and power sources during zebrafish epiboly. We also found that the incompressible yolk displayed stereotyped laminar flows and low but measurable mechanical energy dissipation, suggesting a novel morphogenetic mechanism by which internal flows convey a passive transmission of cortical forces leading to tissue deformation. Our simulations and experimental interferences into E-YSL contractility (*msn1* yolk morphants) (**Figure 7**) further support that the coordinated action of cortical elements (local contractility at the E-YSL and differential tension between the EVL and the yolk surface) and passive viscous flows in the yolk is instrumental in the mechanical implementation of epiboly movements (**Figure 6b**). Local surgical detachment of the EVL and the yolk contact edge in *Fundulus* (Betchaku & Trinkaus, 1978) results in E-YSL faster progression towards the vegetal pole (as no resistance by the EVL was placed to its forward movement) and EVL cells retraction indicating that the EVL/yolk contact is under tension. This last outcome has also been observed for zebrafish (Behrndt et al., 2012). Thus, the EVL, after 50% epiboly appears to limit the speed of epiboly progression resisting to deformation. Yet, an active role of the EVL before reaching the equator, and a mechanical input of DCs ingression (Trinkaus, 1963) (Warga & Kimmel, 1990) (Concha & Adams, 1998) (Koppen et al., 2006) may be necessary to refine the process.

How the increased stiffness at the yolk cortex is achieved? Why is the yolk cortex stiffer than the EVL? Why does its stiffness increase as epiboly progresses? We could speculate that the EVL cells could easily respond to nearby pulling forces flattening passively, while the yolk, on the contrary, has no way to increase its surface area. As a result, tension would accumulate at the yolk membrane as epiboly progresses, which indirectly would lead to an overall progressive reduction of stiffness of the EVL. Indeed, when we artificially increased contractility in the YSL by microsurgery, we observed that nearby EVL cells deformed more than faraway ones, while the vegetal part of the myosin ring did not deform (see **Figure 6A**). On the other hand, we have not

yet explored in quantitative terms the motors involved or the roles that microtubules or actomyosin flows may have in promoting epiboly movements. This would require developing specific analytical protocols as the hydrodynamic method, as such, does not provide any information about the physical mechanism that generates the stresses. Modeling making use of the measured stresses may be employed as input to define the roles for microtubule bundles or biofilaments and to predict their functional roles.

Local tensional stresses and force passive transmission with elastic and viscous components in an incompressible medium provide a simple physical description for the mechanical control of morphogenetic movements. This biological logic appears to be widespread and it applies, for instance, to the folding of the epithelia in the early *Drosophila* embryo during gastrulation, where stresses generated at the surface integrate with the hydrodynamic properties of the interior to transmit force (He et al., 2014). We propose that hydrodynamics may be key for the comprehension of the biomechanics of multiple morphogenetic processes.

METHODS

Zebrafish handling and maintenance, zebrafish lines and mRNA injection

Adult fish were maintained under standard conditions. Collected embryos were grown at 28.5 ºC in E3 embryo medium (Westerfield, 2000) and staged according to morphology as described (Kimmel et al., 1995). AB and TL wild type backgrounds were used throughout this study. Membrane-GFP transgenic Tg (β-*actin:m-GFP*) animals (Cooper, Szeto et al., 2005) were provided by Lilianna Solnica-Krezel and Myosin-EGFP transgenic Tg (β-*actin:myl 12.1-e-GFP*) fish (Behrndt et al., 2012) were supplied by Carl-Philipp Heisenberg. A DNA construct encoding for Lifeact-GFP (Riedl, Crevenna et al., 2008) and cloned in a zebrafish expression vector was kindly provided by Erez Raz. mRNA was *in vitro* synthesized (mMessagem Machine kit, Ambion) and injected into the yolk at one- or 512-cell stages (150 pg) as described (Westerfield, 2000).

To create a condition where E-YSL actomyosin contraction will be blocked we employed Misshapen 1 yolk morphants (Koppen et al., 2006). The *msn1 MO-splice* (5'-ACACACAACT TACccttaaagtgga-3') morpholino that targets the exon 1/intron 1

boundary of the pre-mRNA (Heasman, 2002) was used (kind gift of Antonio Jacinto). We injected 8 ng of the morpholino in the E-YSL at the 1000-cell stage on Tg (β-*actin:m-GFP*) embryos. As previously described (Koppen et al., 2006), half of the injected embryos showed a delay in the epiboly of the DCs and the EVL. To image the internal yolk granules, we obtained medial sections using two-photon microscopy as described below. The velocity fields generated with MatPIV were subjected to analysis by HR.

Electron microscopy

Embryos were dechorionated manually and fixed overnight at 4 ºC with 2 % PFA, 2.5 % glutaraldehyde in PB. They were post fixed in 1 % osmium tetroxide with 0.08 % potassium ferrocyanide, gradually dehydrated through an acetone series, infiltrated in EPON overnight and polymerized for 48 h at 60 °C. Ultrathin sections (50 nm thick) were cut on an ultra microtome Ultracut UC6 (Leica microsystems, Vienna). Images were acquired in a JEOL 1010 electron microscope at 80 kV equipped with a Megaview III CCD camera.

Live Imaging

Embryos were manually dechorionated and mounted in 0.5 % low melting agarose in E3 embryo medium in glass bottom Petri dishes (MatTek, No. 1.5 cover glass) for imaging in both laser scanning and spinning disk confocal microscopy, and in lumox dishes (Starstedt) for two-photon microscopy.

To image the internal yolk granules, medial sections (350 µm depth from the yolk cell surface) were collected from Tg (β-*actin:mGFP*) embryos using a Leica SP5 two-photon microscope equipped with a mode-locked near-infrared MAITAI Laser (Spectra-Physics) tuned at 900 nm, with non-descanned detectors and with a 25 X / 0.95 water-dipping objective. Images were scanned at 200Hz and frames were averaged three times. Stacks of 30 µm, 10 µm step-size, were collected every 2 minutes.

To visualize the surface of the yolk Tg (β-*actin:mGFP*) embryos were imaged in a Zeiss LSM700 confocal microscope with a 63 X / 1.4 oil objective. Stacks of 25 µm, step size of 0.2 µm were acquired.

To study the kinematics of the membrane, dechorionated embryos were incubated in 100 µg/ml lectin-TRITC (Sigma L1261) for 5 minutes at the sphere stage, 50 % or 85 % epiboly, rinsed and mounted for imaging. Images were acquired in a Zeiss LSM 700 confocal microscope with a 40 X / 1.3 oil immersion objective. Stacks of 20 µm, 0.39 µm step size, were acquired every 30 seconds.

A PIV analysis (see below) was applied to time-lapse movies to estimate the velocity field at each time point.

To simultaneously label the E-YSL cortical actin and the membrane, Lifeact-GFP mRNA was injected at 1-cell stage embryos and they were incubated in lectin-TRITC as mention above. Images were collected using a Zeiss LSM 700 confocal microscope with a 63 X / 1.4 oil objective, stack of 11 µm, step size of 0.3 µm.

Image analysis

Most image analyses were performed using Fiji (http://pacific.mpi-cbg.de) and Matlab (Mathworks). To obtain velocity fields through PIV we applied the MatPIV software package written by Johan Kristian Sveen in Matlab (Supatto et al., 2005).

Laser Surgery Experiments and Retraction Analysis

Laser surgery of the actomyosin cortex was performed with a pulsed UV laser (355 nm, 470 ps per pulse) by inducing plasma-mediated ablation as described before (Colombelli et al., 2009). To compare the cortical tension in the AV and CC directions at the E-YSL at different stages, a 20 µm-laser line containing 50 pulses was scanned 5 times at a frequency of 800 Hz, parallel and perpendicular to the EVL front, centering the cut at a distance of about 20 µm, through a 63 X / 1.2 W objective lens. Fluorescence imaging was performed through a custom spinning Nipkow disc unit equipped with a 488 nm laser line and a Hamamatsu ORCA CCD camera, acquiring at 1.5 frames per second.

The same type of laser ablation regime (same laser line length, same pulsed UV laser settings) was applied to validate the AV surface gradient of tension revealed by the regression analysis. This time, only cuts parallel to the EVL were performed at 0, 10, 20, 40 and 60 µm of the EVL border, and at different epiboly stages (50 %, 60-70 % and 80-90 % epiboly).

In all cases, to estimate the tensions, we followed the accepted assumption that the tension of the actomyosin cortex before the laser cut is proportional to the outward velocity of the immediate recoil (Grill, 2011). Retraction analysis was performed as follows: first, from the microscopic video time-lapse recordings of the laser cuts, a region of 160 x 160 pixels was cropped and rotated so the cuts were centered and positioned horizontally. 160 pixels correspond to the apparent length of the original cuts. We then applied a PIV analysis (see Image Analysis) to measure displacements from frame to frame. We applied interrogation windows of 64 square pixels with ¾ overlap generating a 7 x 7 grid. From these grids, we averaged the vertical components of the displacement vectors of the three upper and lower rows and calculated the retraction speed V from their difference.

Quantification and Statistics

Yolk granules kinematics

From the velocity fields measured by PIV in the medial plane of three sibling embryos, we estimated the speed as an average over 10 frames, every 10 frames. We also computed the vorticity of the coarse-grained velocity field and used its maximum absolute value to position the vortex centroid.

Kinematics of the membrane

The velocity component along the AV axis obtained from lectin-label embryos was averaged from parallel rows and consecutive time points at different stages. To compare the different movies, velocities were normalized to the velocity of the margin of the EVL.

Laser cuts

To compare the cortical tension in the AV and CC directions at the E-YSL at different stages, we calculated the mean recoil velocities for each perpendicular direction in each stage and tested the statistical significance of their inequality using the Wilcoxon rank sum test. To quantify the AV surface gradient of tension, we normalized the recoil velocities at each distance from the EVL margin to the recoil velocity at 20 μm distance and tested the statistical significance of the gradient using the Wilcoxon rank sum test.

Cortical tension measurements with Atomic Force Microscopy

Zebrafish epiboly embryos were manually dechorionated and mounted for AFM as follow: small holes of approximately twice the embryo size in diameter and half the embryo size in depth were made with thin forceps in an embryo medium 2 % agarose layer prepared in 35 mm Petri dishes. Embryos were placed in the holes made in the agarose layer and tightly held by surrounding them with 0.5 % low melting agarose. They were rotated to probe the region of interest by AFM (e.g. E-YSL or the vegetal pole).

The cortical tension of the embryos was measured with a custom-build atomic force microscope (AFM) attached to an inverted optical microscope (TE2000, Nikon, Tokyo, Japan) using a previously described method (Alcaraz, Buscemi et al., 2003). The embryos were probed with a spherical polystyrene bead 4.5 μm in diameter attached to a Si_3N_4 cantilever with a nominal spring constant of 0.01 N/m (Novascan, Ames, IA). Force-indentation (F-h) curves were recorded in two different regions of the yolk surface. Each region was probed in five different points located at the center and the corners of a 10 μm x 10 μm square.

The vertical displacement of the AFM cantilever (z) was measured with strain gauge sensors coupled to the piezo-actuators. The cantilever deflection (d) was recorded by a quadrant photodiode using the optical lever method. The slope of a d-z curve obtained from a bare region of the coverslip was used to calibrate cantilever deflection. The cantilever spring constant (k) was determined by the thermal fluctuations method. The force (F) on the cantilever was computed as $F = k \cdot d$. In each measurement point, five force-displacement (F-z) curves were acquired by ramping the cantilever at 1 Hz with a peak-to-peak amplitude of 5 μm (velocity = 10 μm/s) up to a maximum indentation of ~2 μm. The indentation of the sample (h) was computed as $h = (z - z_c) - (d - d_{off})$, where z_c is the position of the contact point and d_{off} is the offset of the photodiode.

Force curves acquired on embryos were interpreted in terms of a "liquid balloon" model consisting of an elastic cortex with cortical tension T_c enclosing a viscous liquid. Assuming a small indentation compared to the size of the embryo, force increases proportionally with indentation (Krieg et al., 2008, Lomakina et al., 2004) as

$$F = 4\pi T_c [(R_b / R_e) +1)] h \quad (3)$$

Where R_b is the radius of the bead and R_e is the radius of the embryo. Since the radius of the embryos as estimated by microscopy images (~ 350 μm) is two orders of magnitude larger than that of the bead (2.25 μm), this equation can be approximated as

$$F = 4\pi T_c h \quad (4)$$

T_c was computed for each F-h curve by non-linear least-squares fitting (Matlab, MathWorks). For statistical analysis, the cortical tension in each embryo region was taken as the average value of T_c computed from the F-h curves recorded at the five different measurement points.

The "liquid balloon" model has been previously described (Ishihara & Sugimura, 2012) and has been employed to estimate cortical tension of leucocytes by micropipette aspiration. This model has been extended to spherical cells indented with a microbead by means of micropipettes (Lomakina et al., 2004), and more recently applied to compute the cortical tension of spherical progenitor cells from gastrulating zebrafish embryos indented with spherical AFM tips 5 μm in diameter (Krieg et al., 2008). Here we adapted this AFM technique to measure T_c of zebrafish whole embryos. Although the "liquid balloon" model equation assumes small sample deformations, as previously reported (Krieg et al., 2008), we found a proportional F-h relationship up to indentations close to the radius of the microbead. Taking into account the linear behavior of the force curves and the sensitivity of parameter estimation, we fitted the "liquid balloon" model to the whole indentation range of our measurements to obtain a robust estimation of T_c.

The force-indentation curves recorded in each of the two regions exhibited a proportional relationship (**Figure 5c**), supporting the liquid-droplet model. The model fitted all the data very well ($R^2 > 0.999$). To evaluate the dependence of T_c on the velocity of the cantilever, two additional sets of five F-h curves were acquired at 3 μm/s and 30 μm/s in the last measurement point. Although T_c increased by 13 % ($p < 0.01$, t-test) when the cantilever velocity was reduced from 10 μm/s to 3 μm/s, no significant change was observed from 10 μm/s to 30 μm/s. This weak dependence of T_c on cantilever velocity provides further support to the interpretation of this parameter computed by AFM as the cortical tension in the embryo.

Rheology of the cortex with Atomic Force Microscopy

The viscoelastic properties of the cortex were measured in 5 embryos with AFM by applying a low amplitude (100 nm) multifrequency oscillation composed of sinusoidal waves of different frequencies (Alcaraz et al., 2003). An effective complex modulus $g^*(f)$ was computed in the frequency domain as

$$g^*(f) = [F(f) / h(f)] - ifb \quad (5)$$

where i is the imaginary unit and $F(f)$ and $h(f)$ are the frequency (f) spectra of force and indentation, respectively. The term b is the correction for the viscous drag on the cantilever computed from oscillations applied above the surface. $g^*(f)$ was separated into real and imaginary parts as $g^*(f) = g'(f) + ig''(f)$. $g'(f)$ is the elastic modulus and is a measure of the elastic energy stored and recovered per cycle of oscillation. $g''(f)$ is the viscous modulus that accounts for the dissipated energy. The loss tangent was also computed as $g''(f) / g'(f)$, which is an index of the solid-like (<1) or liquid-like (>1) behavior of the material.

To compare the stiffness of the embryo with that of other biological materials we also computed the complex shear modulus ($G^*(f) = G'(f) + iG''(f)$) assuming the contact model of an equivalent homogeneous half-space. Transforming Eq. 43 to the frequency domain, G* can be computed as

$$G^*(f) = (1-\nu^2) / [4 (Rh_o)^{1/2}] \cdot [F(f) / h(f)] - ifb \quad (6)$$

where h_o is the operating indentation (~ 0.5 μm).

Rheology of the yolk measured by particle tracking.

The viscoelastic behavior of the yolk was assessed by recording thermal fluctuations of microinjected fluorescent nanoparticles (radius a = 100 nm, FluoSpheres F8811, Life Technologies). Two hours after microinjection, the embryos were placed on the stage of a confocal inverted microscope and images of nanoparticles were recorded for 26 s at a sampling rate of 25 Hz. The position of the centroid of the particles and the trajectories of the particles were determined with ImageJ. The two-dimensional mean square displacement (MSD) of each particle was computed with custom-made software (Daniels et al., 2006) (Wirtz, 2009) as

$$\langle \Delta r^2(\Delta t) \rangle = \langle [x(t + \Delta t) - x(t)]^2 + [y(t + \Delta t) - y(t)]^2 \rangle \quad (7)$$

where t is the elapsed time and Δt, the time lag. In a pure viscous liquid MSD increase inversely with viscosity (ν) according to the Stokes-Einstein relationship

$$\langle \Delta r^2(\Delta t) \rangle = 4k_B T \Delta t / 6 \pi \nu a \quad (8)$$

where T is the absolute temperature. The viscosity of the yolk was calculated by fitting this equation to the MSD data.

ACKNOWLEDGEMENTS

In first place all authors like to acknowledge the essential conceptual and experimental contribution of Philippe-Alexandre Pouille, who passed away during the process of revision and publication of this manuscript. We like to dedicate this work to his memory.

We thank Jacques Prost for a thorough analysis of the HR methodology from a theoretical point of view. We also thank the Confocal Microscopy Unit from IBMB-PCB, the Advanced Digital Microscopy Core Facility from IRB Barcelona, Xavier Esteban and members of the EMB laboratory for continuous support. We are grateful to Javier Buceta, Carolina Minguillón, Emmanuel Farge, Damian Brunner, Katerina Karkali and Carla Prat for reading earlier versions of this manuscript and John P. Trinkaus for inspiring work. The Consolidated Groups Program of the Generalitat de Catalunya and DGI and Consolider Grants from the Ministry of Economy and Competitivity of Spain to EMB and DN supported this work.

AUTHOR CONTRIBUTION

AHV and MM performed all biological tests; PAP designed the modeling and the regression analysis; JC, AHV, MM and PAP performed the laser cuts and data refinement; TL and DN provided the AFM and particle tracking rheology data; ST and IP overview the hydrodynamic analysis and code implementation and EMB designed the study, analyzed the data and wrote the paper. AHV, MM and PAP contributed equally to the study. All authors discussed the results and commented on the manuscript.

COMPETING FINANCIAL INTERESTS

The authors declare no competing financial interests.

REFERENCES

Aigouy B, Farhadifar R, Staple DB, Sagner A, Roper JC, Julicher F, Eaton S (2010) Cell flow reorients the axis of planar polarity in the wing epithelium of Drosophila. Cell 142: 773-86

Alcaraz J, Buscemi L, Grabulosa M, Trepat X, Fabry B, Farre R, Navajas D (2003) Microrheology of human lung epithelial cells measured by atomic force microscopy. Biophysical journal 84: 2071-9

Behrndt M, Salbreux G, Campinho P, Hauschild R, Oswald F, Roensch J, Grill SW, Heisenberg CP (2012) Forces driving epithelial spreading in zebrafish gastrulation. Science 338: 257-60

Betchaku T, Trinkaus JP (1978) Contact relations, surface activity, and cortical microfilaments of marginal cells of the enveloping layer and of the yolk syncytial and yolk cytoplasmic layers of fundulus before and during epiboly. J Exp Zool 206: 381-426

Butcher DT, Alliston T, Weaver VM (2009) A tense situation: forcing tumour progression. Nat Rev Cancer 9: 108-22

Campinho P, Behrndt M, Ranft J, Risler T, Minc N, Heisenberg CP (2013) Tension-oriented cell divisions limit anisotropic tissue tension in epithelial spreading during zebrafish epiboly. Nat Cell Biol 15: 1405-14

Cartwright JH, Piro O, Tuval I (2009) Fluid dynamics in developmental biology: moving fluids that shape ontogeny. HFSP J 3: 77-93

Cheng JC, Miller AL, Webb SE (2004) Organization and function of microfilaments during late epiboly in zebrafish embryos. Dev Dyn 231: 313-23

Colombelli J, Besser A, Kress H, Reynaud EG, Girard P, Caussinus E, Haselmann U, Small JV, Schwarz US, Stelzer EH (2009) Mechanosensing in actin stress fibers revealed by a close correlation between force and protein localization. J Cell Sci 122: 1665-79

Concha ML, Adams RJ (1998) Oriented cell divisions and cellular morphogenesis in the zebrafish gastrula and neurula: a time-lapse analysis. Development 125: 983-94

Cooper MS, Szeto DP, Sommers-Herivel G, Topczewski J, Solnica-Krezel L, Kang HC, Johnson I, Kimelman D (2005) Visualizing morphogenesis in transgenic zebrafish embryos using BODIPY TR methyl ester dye as a vital counterstain for GFP. Dev Dyn 232: 359-68

Daniels BR, Masi BC, Wirtz D (2006) Probing single-cell micromechanics in vivo: the microrheology of C. elegans developing embryos. Biophys J 90: 4712-9

Desprat N, Supatto W, Pouille PA, Beaurepaire E, Farge E (2008) Tissue deformation modulates twist expression to determine anterior midgut differentiation in Drosophila embryos. Dev Cell 15: 470-7

Discher DE, Mooney DJ, Zandstra PW (2009) Growth factors, matrices, and forces combine and control stem cells. Science 324: 1673-7

Evans E, Yeung A (1989) Apparent viscosity and cortical tension of blood granulocytes determined by micropipet aspiration. Biophys J 56: 151-60

Fujimura Y, Inoue M, Kondoh H, Kinoshita S (2007) Measurement of Micro-Elasticity within a Fertilized Egg by Using Brillouin Scattering Spectroscopy. Journal of Korean Physical Society 51: 854

Goldstein RE, Tuval I, van de Meent JW (2008) Microfluidics of cytoplasmic streaming and its implications for intracellular transport. Proc Natl Acad Sci U S A 105: 3663-7

Grashoff C, Hoffman BD, Brenner MD, Zhou R, Parsons M, Yang MT, McLean MA, Sligar SG, Chen CS, Ha T, Schwartz MA (2010) Measuring mechanical tension across vinculin reveals regulation of focal adhesion dynamics. Nature 466: 263-6

Grill SW (2011) Growing up is stressful: biophysical laws of morphogenesis. Curr Opin Genet Dev 21: 647-52

He B, Doubrovinski K, Polyakov O, Wieschaus E (2014) Apical constriction drives tissue-scale hydrodynamic flow to mediate cell elongation. Nature

Heasman J (2002) Morpholino oligos: making sense of antisense? Dev Biol 243: 209-14

Ishihara S, Sugimura K (2012) Bayesian inference of force dynamics during morphogenesis. J Theor Biol 313: 201-11

Keller R, Davidson LA, Shook DR (2003) How we are shaped: the biomechanics of gastrulation. Differentiation; research in biological diversity 71: 171-205

Kiehart DP, Galbraith CG, Edwards KA, Rickoll WL, Montague RA (2000) Multiple forces contribute to cell sheet morphogenesis for dorsal closure in Drosophila. J Cell Biol 149: 471-90

Kimmel CB, Ballard WW, Kimmel SR, Ullmann B, Schilling TF (1995) Stages of embryonic development of the zebrafish. Dev Dyn 203: 253-310

Koppen M, Fernandez BG, Carvalho L, Jacinto A, Heisenberg CP (2006) Coordinated cell-shape changes control epithelial movement in zebrafish and Drosophila. Development 133: 2671-81

Krieg M, Arboleda-Estudillo Y, Puech PH, Kafer J, Graner F, Muller DJ, Heisenberg CP (2008) Tensile forces govern germ-layer organization in zebrafish. Nature cell biology 10: 429-36

Lecuit T, Lenne PF, Munro E (2011) Force generation, transmission, and integration during cell and tissue morphogenesis. Annual review of cell and developmental biology 27: 157-84

Lepage SE, Bruce AE (2010) Zebrafish epiboly: mechanics and mechanisms. The International journal of developmental biology 54: 1213-28

Lomakina EB, Spillmann CM, King MR, Waugh RE (2004) Rheological analysis and measurement of neutrophil indentation. Biophysical journal 87: 4246-58

Martin AC (2010) Pulsation and stabilization: contractile forces that underlie morphogenesis. Dev Biol 341: 114-25

Niwayama R, Shinohara K, Kimura A (2011) Hydrodynamic property of the cytoplasm is sufficient to mediate cytoplasmic streaming in the Caenorhabditis elegans embryo. Proceedings of the National Academy of Sciences of the United States of America 108: 11900-5

Popgeorgiev N, Bonneau B, Ferri KF, Prudent J, Thibaut J, Gillet G (2011) The apoptotic regulator Nrz controls cytoskeletal dynamics via the regulation of Ca2+ trafficking in the zebrafish blastula. Dev Cell 20: 663-76

Pouille PA, Ahmadi P, Brunet AC, Farge E (2009) Mechanical signals trigger Myosin II redistribution and mesoderm invagination in Drosophila embryos. Sci Signal 2: ra16

Rauzi M, Lecuit T (2009) Closing in on mechanisms of tissue morphogenesis. Cell 137: 1183-5

Rawson DM, Zhang T, Kalicharan D, Jongebloed WL (2000) Field emission scanning electron microscopy and transmission electron microscopy studies of the chorion, plasma membrane and syncytial layers of the gastrula□stage embryo of the zebrafish Brachydanio rerio: a consideration of the structural and functional relationships with respect to cryoprotectant penetration. Aquaculture Research 31: 325-336

Riedl J, Crevenna AH, Kessenbrock K, Yu JH, Neukirchen D, Bista M, Bradke F, Jenne D, Holak TA, Werb Z, Sixt M, Wedlich-Soldner R (2008) Lifeact: a versatile marker to visualize F-actin. Nat Methods 5: 605-7

Rodriguez-Diaz A, Toyama Y, Abravanel DL, Wiemann JM, Wells AR, Tulu US, Edwards GS, Kiehart DP (2008) Actomyosin purse strings: renewable resources that make morphogenesis robust and resilient. HFSP J 2: 220-37

Rohde LA, Heisenberg CP (2007) Zebrafish gastrulation: cell movements, signals, and mechanisms. International review of cytology 261: 159-92

Solnica-Krezel L (2006) Gastrulation in zebrafish -- all just about adhesion? Curr Opin Genet Dev 16: 433-41

Solnica-Krezel L, Driever W (1994) Microtubule arrays of the zebrafish yolk cell: organization and function during epiboly. Development 120: 2443-55

Supatto W, Debarre D, Moulia B, Brouzes E, Martin JL, Farge E, Beaurepaire E (2005) In vivo modulation of morphogenetic movements in Drosophila embryos with femtosecond laser pulses. Proceedings of the National Academy of Sciences of the United States of America 102: 1047-52

Toyama Y, Peralta XG, Wells AR, Kiehart DP, Edwards GS (2008) Apoptotic force and tissue dynamics during Drosophila embryogenesis. Science 321: 1683-6

Trinkaus JP (1963) The cellular basis of Fundulus epiboly. Adhesivity of blastula and gastrula cells in culture. Developmental biology 7: 513-32

Warga RM, Kimmel CB (1990) Cell movements during epiboly and gastrulation in zebrafish. Development 108: 569-80

Weliky M, Oster G (1990) The mechanical basis of cell rearrangement. I. Epithelial morphogenesis during Fundulus epiboly. Development 109: 373-86

Westerfield M (2000) The Zebrafish Book: A Guide for the Laboratory Use of Zebrafish (Danio rerio). Eugene, OR: University of Oregon Press,

Wirtz D (2009) Particle-tracking microrheology of living cells: principles and applications. Annual review of biophysics 38: 301-26

Wolke U, Jezuit EA, Priess JR (2007) Actin-dependent cytoplasmic streaming in C. elegans oogenesis. Development 134: 2227-36

Yamamoto K, Shimada K, Ito K, Hamada S, Ishijima A, Tsuchiya T, Tazawa M (2006) Chara myosin and the energy of cytoplasmic streaming. Plant Cell Physiol 47: 1427-31

Yi K, Unruh JR, Deng M, Slaughter BD, Rubinstein B, Li R (2011) Dynamic maintenance of asymmetric meiotic spindle position through Arp2/3-complex-driven cytoplasmic streaming in mouse oocytes. Nat Cell Biol 13: 1252-8

FIGURE LEGENDS

Figure 1. Epiboly kinematics

(a) Representation of a zebrafish embryo at 70 % epiboly. Animal (A) and vegetal (V) poles and φ (embryo surface - red) and ρ (internal to external axis - green) are indicated. The enveloping layer (EVL) is a single-cell layer (dark grey) that stands at the animal cap surface surrounding the inner deep cells (DCs) (blue). It is attached to the yolk cell membrane (purple). The YSL and Yolk Cytoplasmic Layer (YCL) (yellow) at the periphery and yolk granules fill the yolk cell. Progression of epiboly is represented by a curved black arrow. Geometrical axes are shown in grey. **(b)** Kinematics of the embryo surface. A kymograph of the embryo surface (φ axis) from a Tg (β-*actin:m-GFP*) embryo shows the continuous displacement of the EVL / yolk margin, which accelerates after 50% epiboly, while the yolk cell membrane does not show any shift (see **Video EV1**). **(c)** Theoretical kymograph from 50 % to 70 % epiboly superimposed, between the red lines, on the experimental kymograph **(b)**. Membrane signal intensity is color-coded (blue to red). White arrowheads point to flow lines (black). **(d)** AV velocities, normalized to EVL / yolk margin velocity, were measured by PIV of time-lapse recordings of the surface of lectin-soaked embryos. The plots correspond to three different epiboly stages (30 %, blue; 60 %, red; and 90 %, green). Blue and red arrows point to the width of the E-YSL at 30 and 60 % epiboly respectively (from **Appendix Figure S1)**. **(e)** The yolk cell membrane is highly convoluted (white brackets) ahead of the EVL leading cells and condenses over time. Tg (β-*actin:m-GFP*) embryo at 30 % (left) and 60 % (right) epiboly. Scale bar 25 μm. Inset shows a high magnification of the wrinkled area (arrowhead). Scale bar 10 μm. **(f)** Actin accumulates within wrinkles at the E-YSL. The yolk cell membrane of LifeAct-GFP injected embryos (actin - green) was stained with lectin-TRITC (red) (top). Orthogonal projection of the wrinkled area (bottom). Wrinkles are outlined with a white dotted line. Scale bar 2 μm.

Figure 2. Yolk Flows

(a) Yolk granules flow in stereotyped patterns as epiboly progresses. PIV of time-lapse snapshots imaged by two-photon microscopy of a Tg (β-*actin:m-GFP*) embryo (from **Video EV2**). Upon epiboly onset, yolk granules flow towards the animal pole displaying two internal vortices near the E-YSL. At 50 %, the movement of the yolk

granules halts, but resumes afterwards until the end of epiboly. Animal (A) and vegetal (V) poles are indicated. Scale bar 100 μm. **(b)** Internal yolk content speed (μm/min) at the center of the embryo, over time (min). Inset: Spherical coordinates. The main axis of the sphere is represented by z, from the animal to the vegetal pole. The polar angle is represented by φ and the radial coordinate is denoted ρ. **(c)** Vortex midpoints distance from the center (ρ), over time (min). **(d)** Vortex midpoints position in relation to the φ axis, over time (min). Black lines represent individual measurements. Red lines represent averages. **(e)** Correlation between vortex displacement (blue, average of n=3 embryos) vs. EVL margin displacement (red, average of n = 4 embryos) along the main axis (z), over time (min). Standard errors are displayed. Arrow points to 50 % epiboly.

Figure 3. Hydrodynamics Regression

(**a**) Any cortical surface of living organisms could be considered a structure under tension embedded in viscous fluids, where the stresses in the three dimensions at each point are locally balanced $\partial\sigma_{ij} / \partial x_j = 0$ and the cortex tension τ is at equilibrium $\partial / \partial x_t\ \tau = 0$ (top). Any disequilibrium in this tension ($\partial / \partial x_t\ \tau \neq 0$), e.g. due to the stretching of the cortex surface (graded double-headed arrow), will result in a discontinuity of the shear stress of the surrounding viscous fluid and the induction of flows (green arrows) (bottom). Thus, the measurement of the shear flow of the viscous fluid on both sides of a cortical surface lets inferring the quantitative profile of the surface tension along the cortex, regardless of its elastic properties. **(b)** Representation of an Stokeslet pair, at the limits of a perpendicular section of a planar hydrodynamic active cortex (red shadow), pointing in opposite directions (white arrows) and their associated flow lines (black) and mechanical pressure fields (color-coded). **(c)** Divergence fields of Stokeslet dipoles of opposite magnitudes corresponding to cortical expansion or contraction (left). These dipoles carry an associated mechanical pressure (middle) and power (right). Mechanical power is positive at the central Stokeslet pair that is surrounded by a cortical ring that resists its deformation. **(d)** Pipeline describing the different steps involved in HR. From time-lapse 2D videos (green shadowed in yellow) a set of parameters for the fluid phase (blue) are sequentially acquired through PIV and regression analysis, in particular the fluid stress (shadowed in pink). From these, the relative elastic stress and mechanical power (purple shadowed in pale blue) of the cortex are extracted for different geometrical configurations **(e)** Representation of

the planar cortex (PC) (left) and the spherical cortex (SC) (right) models where the elementary solutions (dots) pointing in opposite directions (pale green arrows) are evenly distributed on a square grid (PC) or symmetrically distributed around the main cylindrical axis of a sphere (N_c = 16) (SC). For the PC model only the external components are shown in one row and one column. For the SC model only the external components are shown in one column.

Figure 4. Epiboly biomechanics

(a) Yolk microrheology. Mean squared displacement (MSD) of thermal fluctuations of fluorescent nanoparticles embedded in the yolk of zebrafish embryos. Solid and dashed black lines are mean ± SE computed from 99 particles. Red line is the fit of the Stokes-Einstein equation. MSD of nanoparticles embedded in the yolk exhibits a proportional dependence on time lag, Δt, consistent with a Newtonian liquid behavior with a viscosity of 129 mPa·s. A linear time dependence of MSD with similar values of yolk viscosity has been recently reported in *Drosophila* (He et al., 2014). Interestingly, the viscosity of the zebrafish yolk is two orders of magnitude lower than that of C. *elegans* embryos (Daniels et al., 2006) and of the cytoplasm of several cell types (Wirtz, 2009). **(b)** Viscoelasticity of the yolk cortex. Effective complex modulus (g^*) measured by indenting the surface of zebrafish embryos with AFM. Red symbols are the elastic modulus (g') and yellow symbols are the viscous modulus (g''), respectively. In all the measured frequencies cortex rheology is dominated by a solid-like behavior with the viscous modulus ~5 times lower that the elastic modulus. No significant frequency dependence was found in the elastic (ANOVA, p = 0.123) and viscous modulus (ANOVA, p = 0.719). **(c)** Flow lines from snapshots of the PIV measurements (at 40, 60 and 80 % epiboly) of a two-photon video time-lapse (from **Video EV4**) of a Tg (β-*actin:m-GFP*) embryo (top). Fitted flow lines using HR ar shown at the bottom. The relative mean square errors (RMSE) of the fitting are displayed as a percentage at the bottom left of each panel. Scale bar 100 μm. **(d)** Mechanical power maps over time obtained by HR of the same embryos as in (**c**) (from **Video EV5**). The RMSE of the power is shown as a percentage at the bottom left of each panel. The mechanical work to produce doming (40 % epiboly) arises mainly at the blastoderm (left); at 60 % epiboly (middle) DCs undergo ingression (red) while the E-YSL resists constriction (blue). At 80 % epiboly (right), the active work leading to the active movement of the

EVL / yolk margin mainly maps at the E-YSL (red) while the blastoderm undergoes elastic resistance (blue). White arrows point to the main observed events. Scale bar 100 μm. **(e)** AV (red) and CC (green) stresses and their differences (blue) normalized values in arbitrary units from the regression analysis (**Video EV6**) were plotted as a function of the φ angle (0-1) along the cortex from animal to vegetal. The equator - dotted yellow line -, yolk surface - purple shadow - and the RMSE of the mechanical pressure as a percentage for each time point are displayed (40 %; 60 %; 80 % epiboly). The CC stress steeps up from animal to vegetal and the AV shows a more complex profile. Their difference changes senses around the EVL / yolk margin.

Figure 5. Experimental validation of epiboly tensional pattern

(a) Correlation between the differential tension (cyan) represented by the recoil velocities differences (μm/s) between CC and AV laser cuts and their difference (blue) calculated by regression analysis at the E-YSL during epiboly (%). The difference values in normalized relative units were fitted applying a constant adjustment ratio at all time points. **(b)** AV tension (averaged recoil velocity in μm/s) in the yolk cortex at different distances from the EVL (0, 10, 20, 40 and 60 μm) and at different epiboly stages (50 %, blue; 60-70 %, red; 80 % epiboly, green). Significant changes are highlighted. **(c)** Probing mechanical parameters of living embryos with AFM. Force-indentation curves recorded at cantilever velocity of 10 μm/s (blue) fitted with a "liquid balloon" model (red). Inset: AFM force-indentation description. **(d)** Averaged values of mean surface tension (pN / μm) on the yolk obtained with AFM at different epiboly stages (left), and the significant difference of tension at 60-70 % epiboly ($p = 0.0245$) between the E-YSL and the vegetal pole (right).

Figure 6. Epiboly is driven by E-YSL contractility and differential surface tensions

(a) Kymograph showing the deformation of the cortex along a segment perpendicular to a laser cut (red line time point) in the E-YSL of a Myosin-GFP transgenic embryo [Tg (β-*actin:myl 12.1-e-GFP*)]. After a rapid opening, an active contraction displaces the cut centroid vegetalward indicating that the EVL is more easily stretched (elastic) than the vegetal yolk cell membrane/cortex. When the gap is closed, the cut center returns to its initial position and the elastic equilibrium is restored. Scale bar 10 μm. **(b)** Proposed model of epiboly progression. The contractile E-YSL and the imbalance of stiffness

between the EVL and the yolk surface account for epiboly progression. The vegetal boundary of the E-YSL is not mechanically free but linked to the tense yolk membrane. The tension originated by constriction of the actomyosin ring (E-YSL) is thus conveyed by the yolk membrane towards the vegetal pole leading to the progression of the less stiff EVL. Passive movements within the yolk arise as a result of force transmission from the surface. **(c)** Dynamic simulation of epiboly based on a single spherical cortex model (SC) considering a gradient of elastic tension from animal to vegetal and a constricting area at the E-YSL (from **Video EV8** - 40 %; 60 %; 80% epiboly). Color-coded mechanical power map normalized values in arbitrary units (positive - red, negative - blue) (left). Flow lines (right). The mechanical power is supplied at the surface and internal vortices and their shift from animal to vegetal are precisely simulated. **(d)** Dynamic simulation of AV and CC stresses normalized values in arbitrary units (from **Video EV9** – 40 %; 65 %; 80 % epiboly) represented as in **Figure 1a**. The AV and CC stresses are equal at the poles, as the epiboly simulation progresses, the CC stress steeps up from animal to vegetal and the difference between CC and AV stresses change sense at the EVL / yolk margin.

Figure 7. Experimental validation of the differential surface tension model

(a) Speed of the EVL advancing front at different epiboly stages (ϕ angle) for two distinct simulated conditions: 1) a difference of elastic tension between the EVL and the yolk associated to a two-phase reduction of the contractile E-YSL width (from 20º to 5º) as epiboly advances (from 50º to 155º) (wild type - blue). The contractile E-YSL width decreases at a slower rate until 80º and shrinks afterwards at a rate 2.25 times faster, and 2) Same assumptions as in 1 but with no shrinkage of the E-YSL (constant 20º) (contractileless - red). **(b)** Experimental values for the EVL advancing front speeds at different epiboly stages (ϕ angle - top) and at different times (bottom) for wild type controls (blue) and Msn1 yolk morphants with reduced E-YSL contractility (red). Experimental profiles closely approach to those inferred in the simulations (compare to **(a)**). **(c)** Timeline showing medial sections and power isolines for wild type (top) and Msn1 yolk morphants (bottom) along epiboly. Mechanical parameters were inferred by HR from experimental velocity fields (**Video EV10**). The RMSE of power is shown as a percentage at each time point. DCs in the Msn1 yolk morphants undergo ingression on schedule at 50 % epiboly (yellow arrow). Importantly, as in wild type controls, the

active work in morphants is detected at the E-YSL (red arrow). This power supply fades away as epiboly slows down and eventually fails. Scale bar 100 μm. **(d)** Tensional profiles normalized values in arbitrary units inferred by HR for wild type at 80 % epiboly and its temporal equivalent (9 hours after egg laying) for Msn1 yolk morphants. The characteristic profiles of longitudinal and latitudinal stresses and the animal to vegetal stress gradient that are built up during epiboly are never properly developed in morphants.

Figure 1

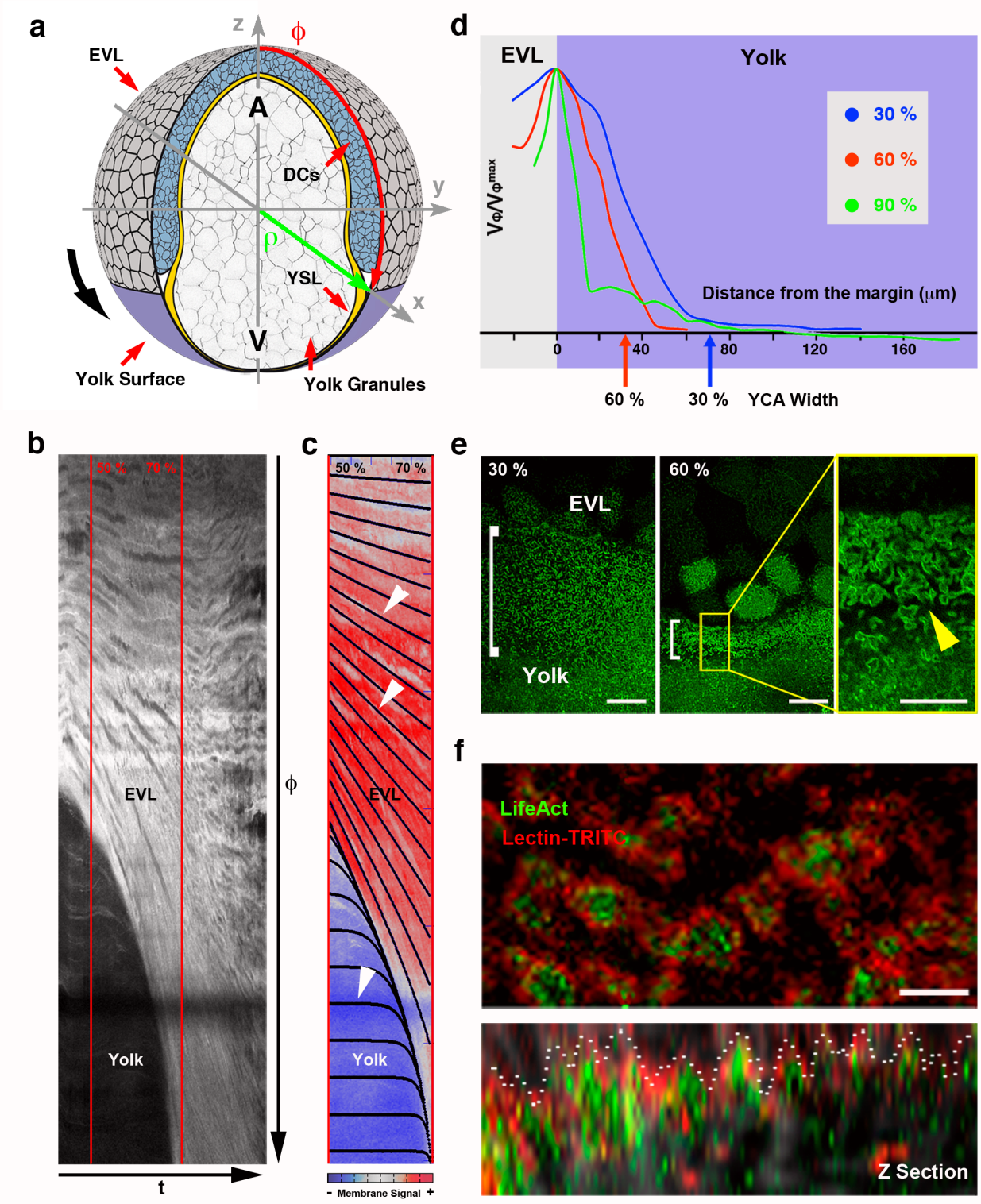
a
z
ϕ
EVL
A
DCs
y
ρ
YSL
x
V
Yolk Surface
Yolk Granules
d
EVL
Yolk
30 %
60 %
90 %
Vϕ/Vϕmax
Distance from the margin (μm)
0
40
80
120
160
60 %
30 %
YCA Width
b
50 %
70 %
EVL
Yolk
ϕ
t
c
50 %
70 %
EVL
Yolk
- Membrane Signal +
e
30 %
EVL
Yolk
60 %
f
LifeAct
Lectin-TRITC
Z Section

Figure 2

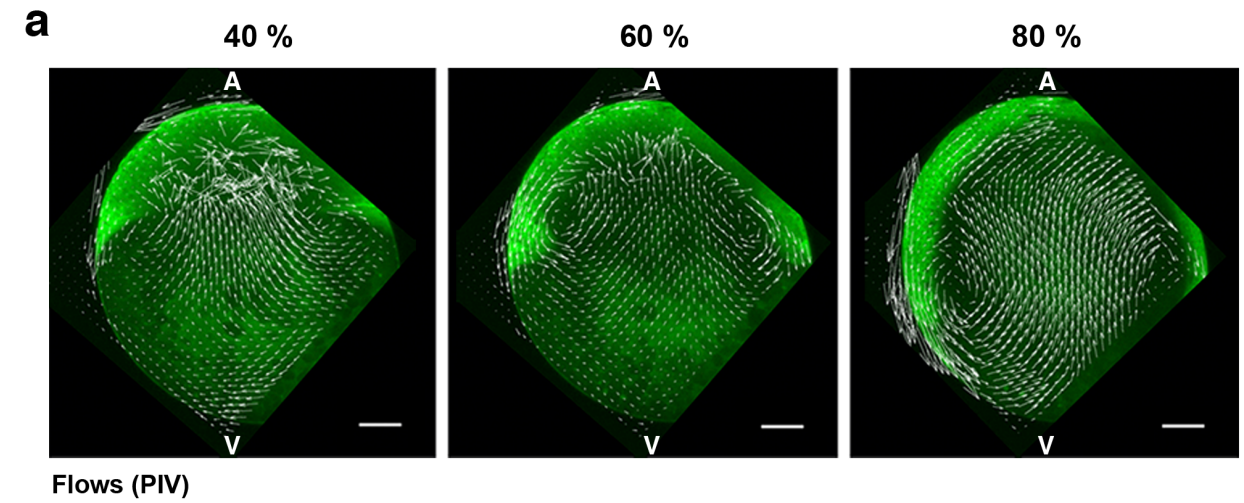
a
40 %
60 %
80 %
A
V
Flows (PIV)

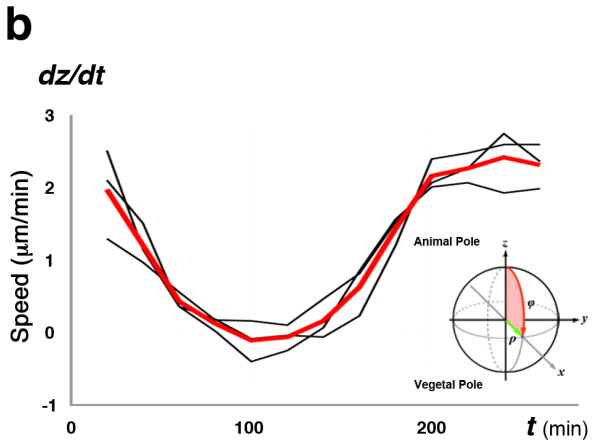
b
dz/dt
Speed (µm/min)
3
2
1
0
-1
0
100
200
t (min)
Animal Pole
Vegetal Pole

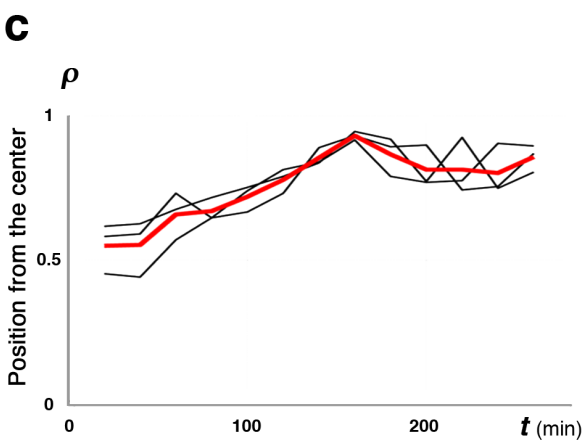
c
ρ
Position from the center
1
0.5
0
0
100
200
t (min)

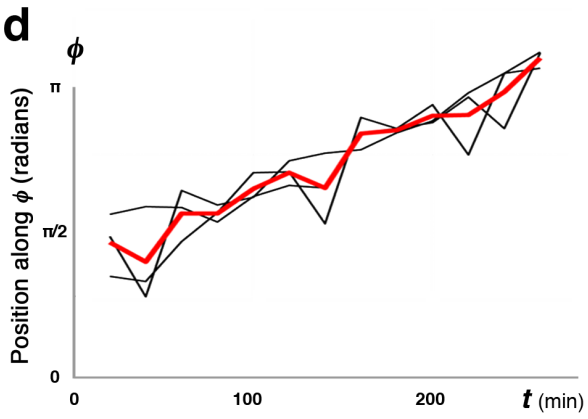
d
ϕ
Position along ϕ (radians)
π
π/2
0
0
100
200
t (min)

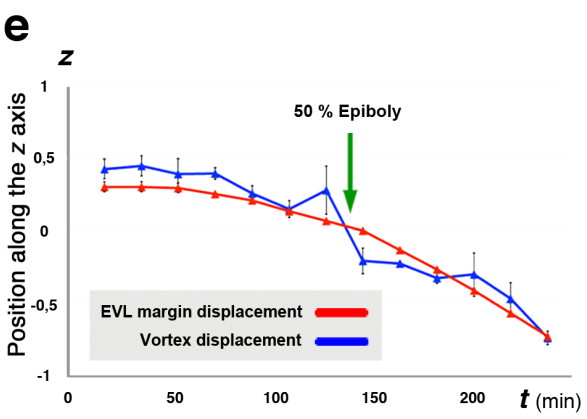
e
z
Position along the z axis
1
0,5
0
-0,5
-1
50 % Epiboly
EVL margin displacement
Vortex displacement
0
50
100
150
200
t (min)

Figure 3

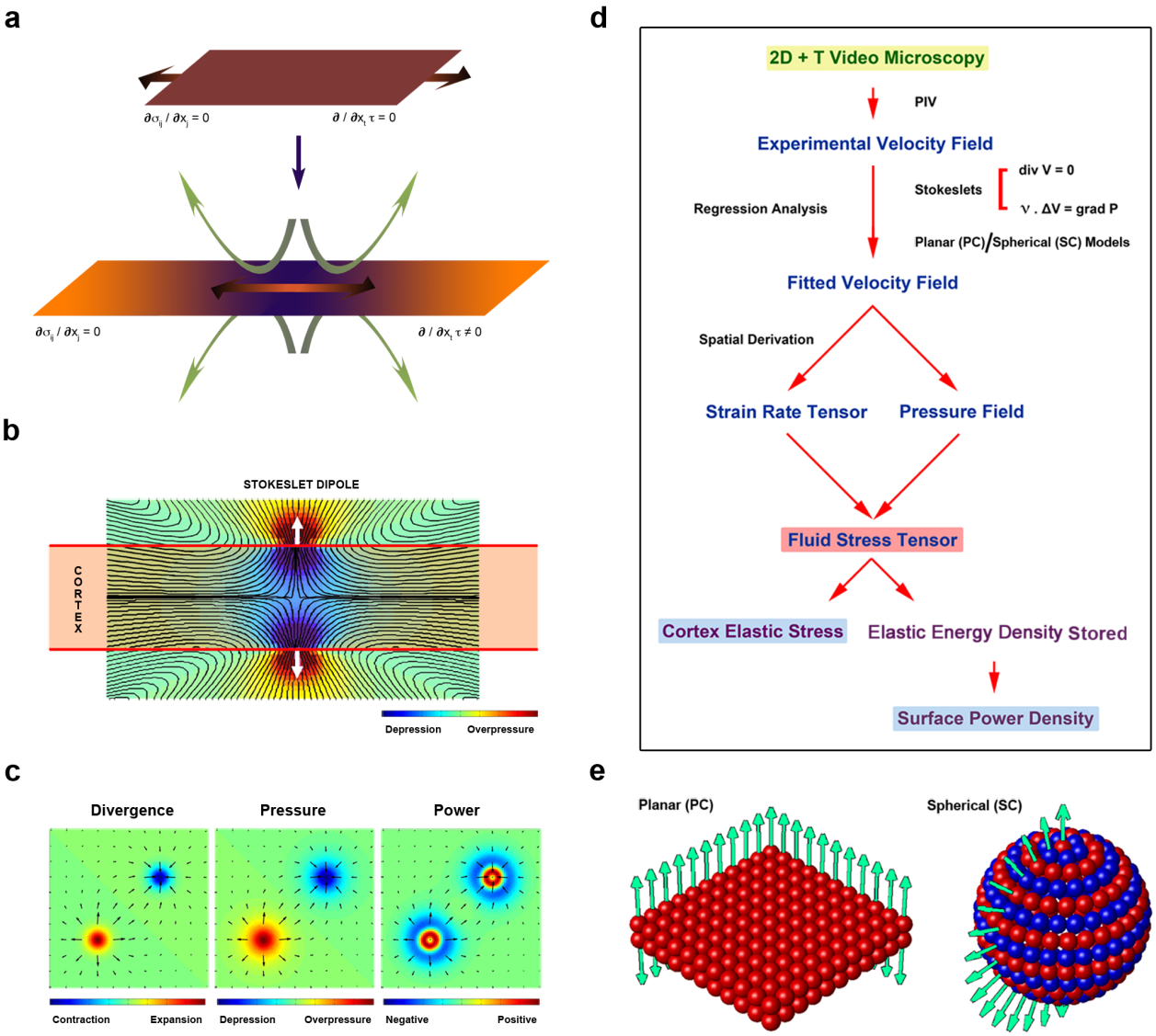
a
$\partial\sigma_{ij} / \partial x_j = 0$
$\partial / \partial x_i \tau = 0$
$\partial\sigma_{ij} / \partial x_j = 0$
$\partial / \partial x_i \tau \neq 0$
b
STOKESLET DIPOLE
CORTEX
Depression
Overpressure
c
Divergence
Pressure
Power
Contraction
Expansion
Depression
Overpressure
Negative
Positive
d
2D + T Video Microscopy
PIV
Experimental Velocity Field
Regression Analysis
Stokeslets
div V = 0
ν . ΔV = grad P
Planar (PC)/Spherical (SC) Models
Fitted Velocity Field
Spatial Derivation
Strain Rate Tensor
Pressure Field
Fluid Stress Tensor
Cortex Elastic Stress
Elastic Energy Density Stored
Surface Power Density
e
Planar (PC)
Spherical (SC)

Figure 4

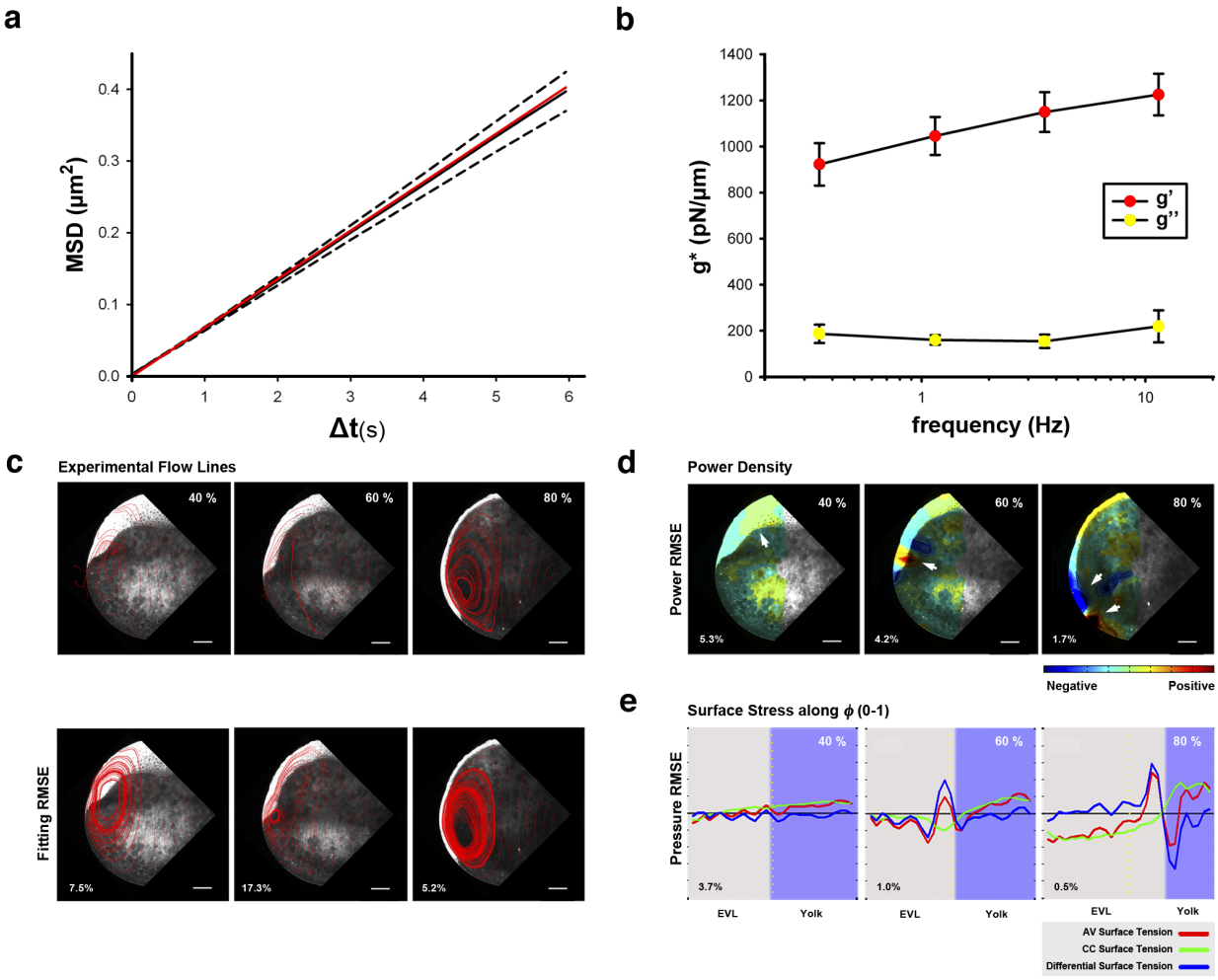
a
MSD (μm²)
Δt(s)
b
g* (pN/μm)
frequency (Hz)
g'
g''
c
Experimental Flow Lines
40 %
60 %
80 %
Fitting RMSE
7.5%
17.3%
5.2%
d
Power Density
Power RMSE
5.3%
4.2%
1.7%
Negative
Positive
e
Surface Stress along ϕ (0-1)
Pressure RMSE
3.7%
1.0%
0.5%
EVL
Yolk
AV Surface Tension
CC Surface Tension
Differential Surface Tension

Figure 5

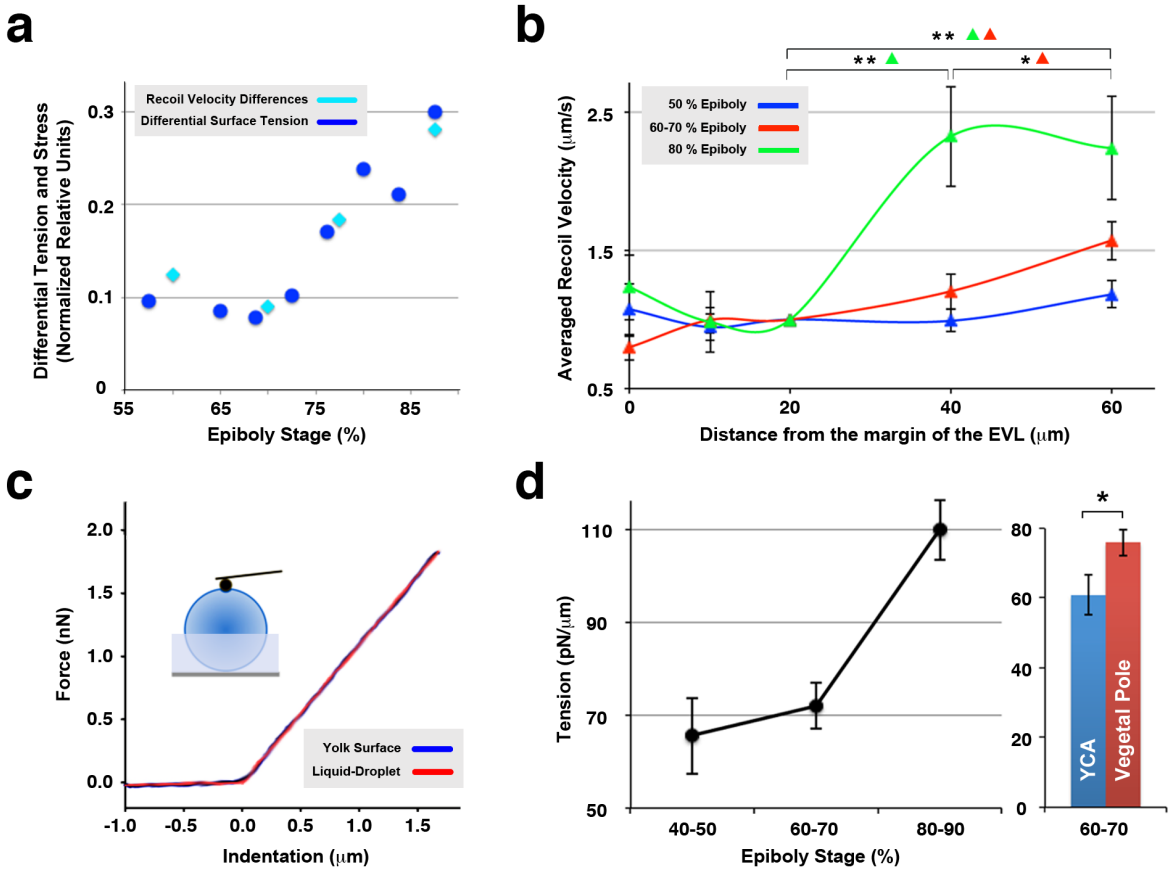
a
Recoil Velocity Differences
Differential Surface Tension
Differential Tension and Stress (Normalized Relative Units)
0.3
0.2
0.1
0
55
65
75
85
Epiboly Stage (%)
b
**
**
*
50 % Epiboly
60-70 % Epiboly
80 % Epiboly
Averaged Recoil Velocity (μm/s)
2.5
1.5
0.5
0
20
40
60
Distance from the margin of the EVL (μm)
c
Force (nN)
2.0
1.5
1.0
0.5
0.0
-1.0
-0.5
0.0
0.5
1.0
1.5
Indentation (μm)
Yolk Surface
Liquid-Droplet
d
Tension (pN/μm)
110
90
70
50
40-50
60-70
80-90
Epiboly Stage (%)
*
80
60
40
20
0
YCA
Vegetal Pole
60-70

Figure 6

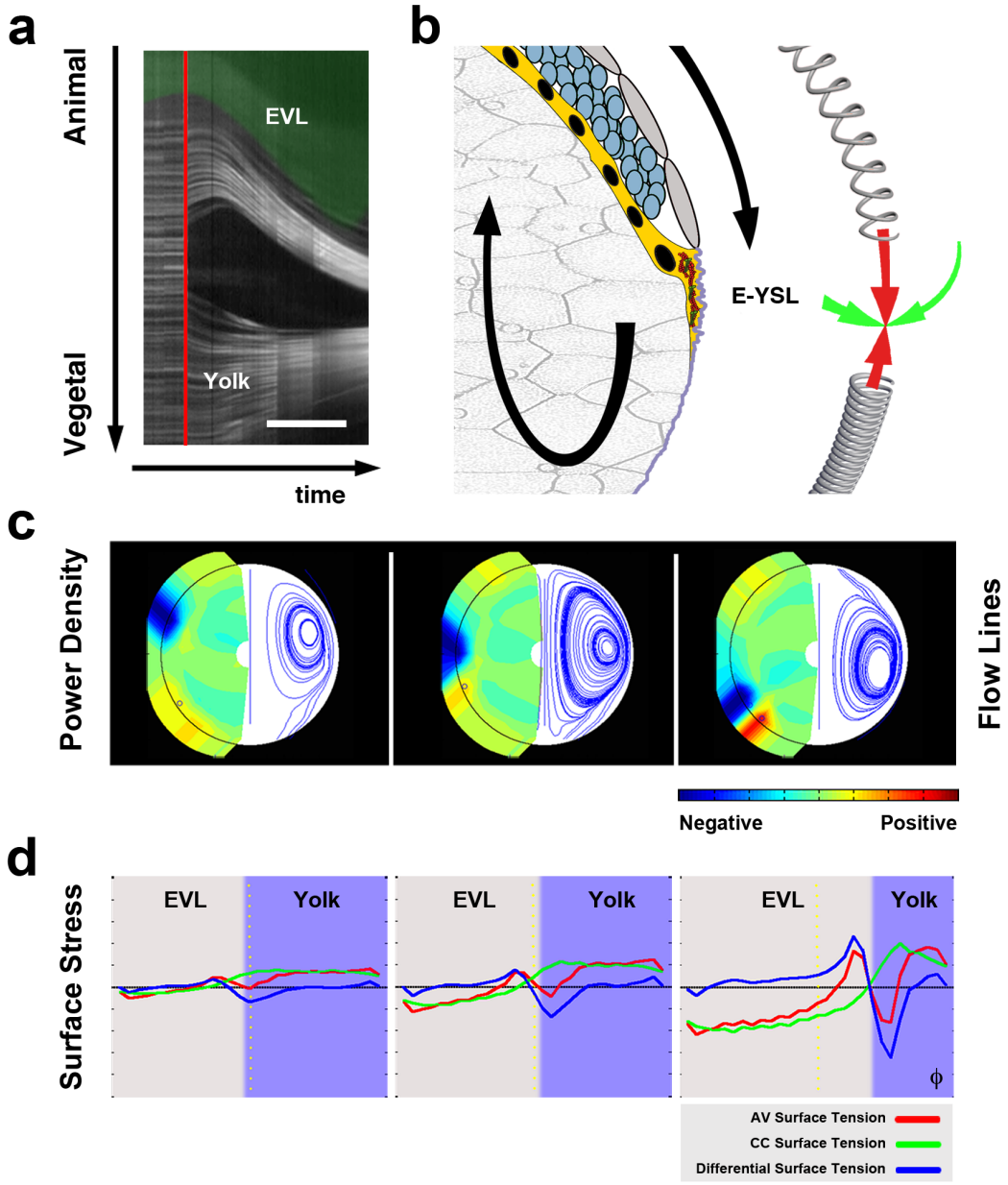
a
Animal
Vegetal
EVL
Yolk
time
b
E-YSL
c
Power Density
Flow Lines
Negative
Positive
d
Surface Stress
EVL
Yolk
EVL
Yolk
EVL
Yolk
ϕ
AV Surface Tension
CC Surface Tension
Differential Surface Tension

Figure 7

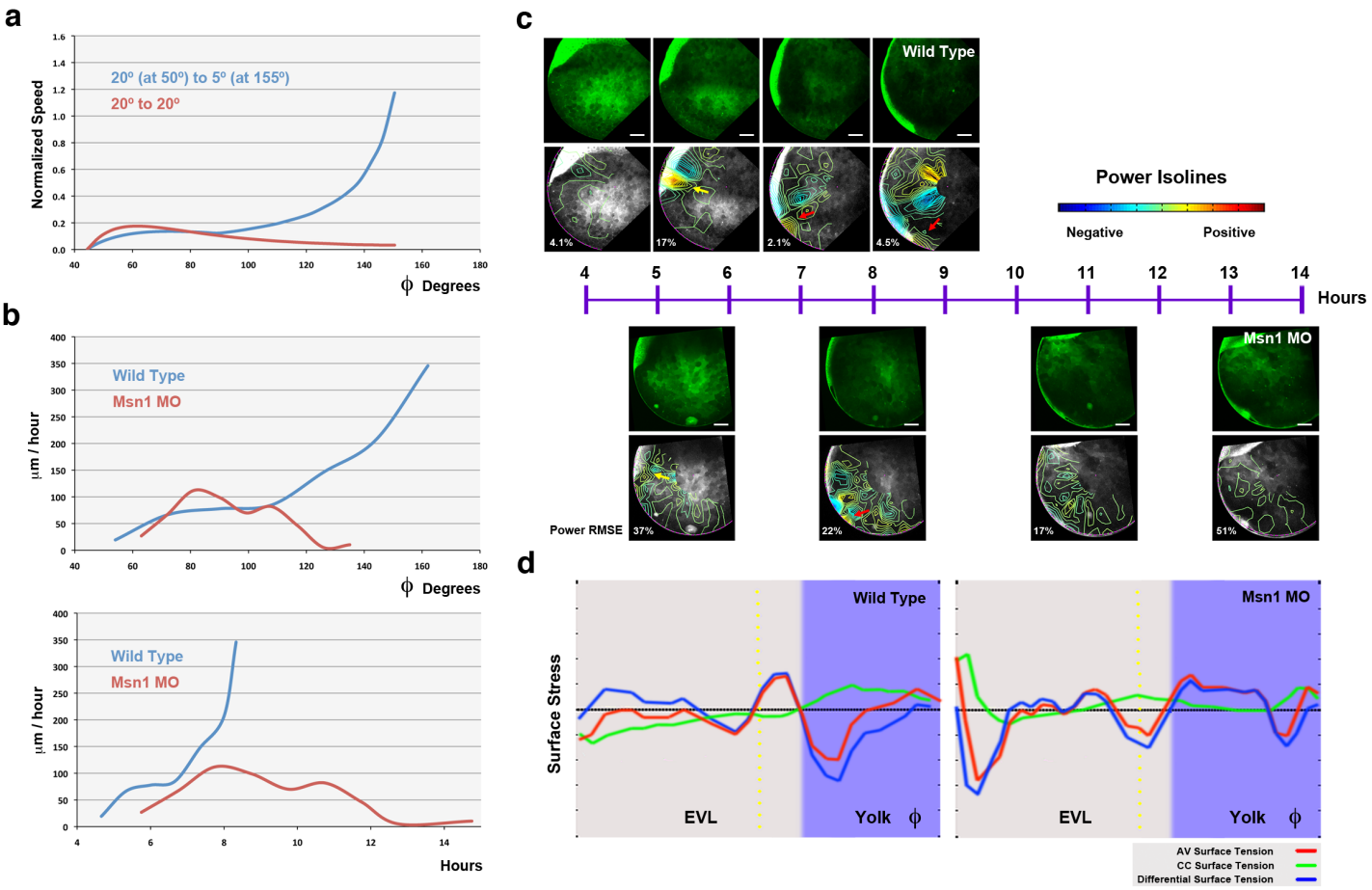
a
Normalized Speed
20º (at 50º) to 5º (at 155º)
20º to 20º
ϕ Degrees
b
µm / hour
Wild Type
Msn1 MO
ϕ Degrees
µm / hour
Wild Type
Msn1 MO
Hours
c
Wild Type
Power Isolines
Negative
Positive
4.1%
17%
2.1%
4.5%
4 5 6 7 8 9 10 11 12 13 14
Hours
Msn1 MO
Power RMSE
37%
22%
17%
51%
d
Surface Stress
Wild Type
Msn1 MO
EVL
Yolk ϕ
EVL
Yolk ϕ
AV Surface Tension
CC Surface Tension
Differential Surface Tension